Investigation of PR and TMI Version 6 and Version 7 Rainfall Algorithms in Landfalling Tropical Cyclones Relative to the NEXRAD Stage-IV Multisensor Precipitation Estimate Dataset

JOSEPH P. ZAGRODNIK AND HAIYAN JIANG

Department of Earth and Environment, Florida International University, Miami, Florida

ABSTRACT

Rainfall estimates from versions 6 (V6) and 7 (V7) of the Tropical Rainfall Measuring Mission (TRMM) precipitation radar (PR) 2A25 and Microwave Imager (TMI) 2A12 algorithms are compared relative to the Next Generation Weather Radar (NEXRAD) Multisensor Precipitation Estimate stage-IV hourly rainfall product. The dataset consists of 252 TRMM overpasses of tropical cyclones from 2002 to 2010 within a 230-km range of southeastern U.S. Weather Surveillance Radar-1988 Doppler (WSR-88D) sites. All rainfall estimates are averaged to a uniform $1/7°$ square grid. The grid boxes are also divided by their TMI surface designation (land, ocean, or coast). A detailed statistical analysis is undertaken to determine how changes to the TRMM rainfall algorithms in the latest version (V7) are influencing the rainfall retrievals relative to ground reference data. Version 7 of the PR 2A25 is the best-performing algorithm over all three surface types. Over ocean, TMI 2A12 V7 is improved relative to V6 at high rain rates. At low rain rates, the new ocean TMI V7 probability-of-rain parameter creates ambiguity in differentiating light rain (≤ 0.5 mm h^{-1}) and non-raining areas. Over land, TMI V7 underestimates stage IV more than V6 does at a wide range of rain rates, resulting in an increased negative bias. Both versions of the TMI coastal algorithm are also negatively biased at both moderate and heavy rain rates. Some of the TMI biases can be explained by uncertain relationships between rain rate and 85-GHz ice scattering.

1. Introduction

The recent release of version 7 (V7) of the Tropical Rainfall Measuring Mission (TRMM) precipitation radar (PR) 2A25 and Microwave Imager (TMI) 2A12 rainfall algorithms presents an opportunity to compare the new version (V7) to the previous release, version 6 (V6). It is commonly accepted that these algorithms perform well on large spatial and temporal scales, but they often have more significant local errors that are problematic on a case-by-case basis. These errors tend to be amplified in tropical cyclones (TCs), which produce anomalously high rain rates that are difficult to capture using passive microwave techniques. Since inland flooding is a major cause of deaths and damages in TCs, satellite precipitation algorithms have the potential to be a valuable tool for forecasters to pinpoint the

location of the heaviest rainfall ahead of a TC landfall, when the storm is still out of range of ground-based radar. Combined algorithms like the TRMM Multisatellite Precipitation Analysis (TMPA; Huffman et al. 2007) also use microwave algorithms similar to the TMI 2A12 as a data source and for calibration. Over the open ocean, satellite-derived precipitation algorithms are the best tool for real-time precipitation analysis. Numerical weather prediction output can also provide rainfall information, but it often has questionable accuracy in convective systems including TCs (Ebert et al. 2007). The main goal of this study is to quantify the errors and sources of bias in the TRMM precipitation algorithms using a surface reference dataset. This study investigates TCs, which represent a specific meteorological regime that is individually selected from the monthly and annual datasets. Interpreting satellite precipitation algorithms for a particular regime can be difficult because the algorithms have higher levels of uncertainty on smaller scales. Biases in the algorithm code that are usually negligible may be accentuated in tropical cyclones. To reduce any bias from a particular storm or geographical region, this study uses

Corresponding author address: Dr. Haiyan Jiang, Dept. of Earth and Environment, Florida International University, 11200 SW 8th St., PC-342B, Miami, FL 33199.
E-mail: haiyan.jiang@fiu.edu

a large dataset of 252 TRMM overpasses of TCs near land, landfalling TCs, and postlandfall TCs across the entire southeastern United States.

Satellite precipitation algorithms are usually divided into three categories: ocean, land, and coast. Ocean algorithms derived from microwave radiometer measurements can use both low-frequency emission-based channels and high-frequency scattering-based channels. Land algorithms can only use the high-frequency scattering channels, as high and variable land surface emissivity combine to mask the emission signature of liquid precipitation. Coastal algorithms rely mostly on scattering-based channels while removing artificial rain signatures associated with different fractions of land and ocean in each microwave footprint (McCollum and Ferraro 2005). Retrieval over land is more difficult without the emission channels, as the scattering signatures characterize processes higher in the cloud that do not directly relate to surface rainfall (Wilheit et al. 2003). Oceanic algorithms are also dependent on the scattering channels to achieve a higher resolution than the emission channels can independently provide. The difference between land and ocean causes fewer uncertainties in the PR algorithm, although variations in the surface cross section can bias the rain rate. Over ocean, the backscatter is related to sea surface wind, while over land, a soil surface and vegetation backscattering model must be used (Seto and Iguchi 2007). The PR's 2.17-cm wavelength (13.8-GHz frequency) also results in attenuation, especially in heavy rainfall (Iguchi et al. 2000).

Version 7 is relatively new, so most previous studies compare version 6 relative to reference data. Studies that use instantaneous data are most relevant to this work, along with seasonal comparisons focusing on the summer, fall, and/or wet season. Jiang and Zipser (2010) used TRMM to examine the contribution of TCs to total TC-season (June–November) precipitation. Across the southeastern United States, both PR V6 and TMPA (3B42) agreed that TCs contribute approximately 5%–20% of total precipitation, with the highest contribution over ocean and lowest inland. When considering just the highest 3B42 rain rates ($>20 \, \mathrm{mm \, h^{-1}}$), the contribution from TCs is 12% over land and 31% over ocean (Prat and Nelson 2013). Wolff and Fisher (2008) evaluated PR and TMI V6 at the TMI footprint scale over land, ocean, and coast at the TRMM Ground Validation (GV) sites. They found that PR V6 underestimates rainfall relative to GV, with the most significant underestimation occurring over land and coast and at rain rates greater than about 10–20 $\mathrm{mm \, h^{-1}}$. The TMI V6 underestimates GV and PR over ocean and coast at both lower and high rain rates but is greater than the PR for $>20 \, \mathrm{mm \, h^{-1}}$ rain rates over land. Amatai et al. (2009) found similar PR

V6 underestimation relative to the National Oceanic and Atmospheric Administration Next-Generation Quantitative Precipitation Estimate (Q2) product including a case study of Hurricane Humberto at landfall. They also determined that the probability density functions (PDF) of PR V6 are single-peaked and shifted toward lower rain rates, implying a greater PR stratiform–convective ratio than the double-peaked Q2 PDFs. The specific uncertainty values of both satellite and ground radar estimates remains unquantified.

Regarding the transition from V6 to V7, Wang et al. (2009) highlighted several known TMI V6 inconsistencies over land, including overestimation in deep convection and underestimation in warm rain regimes relative to PR V6 and rain gauges. Gopalan et al. (2010) describe the steps taken in the TMI V7 land algorithm to correct these issues. Specifically, they added a more comprehensive set of TMI–PR collocations to improve the relationship between TMI rain rates and the 85-GHz channel. Their results show that while TMI V7 improves on the global "wet" bias, it does not reduce regional biases that are driven mostly by surface screening, emissivity, warm rainfall, and deep convection. They also stress that since the TMI algorithm is trained using PR data, it is important to perform validations using an independent dataset. The main changes to PR V7 include several adjustments to the attenuation correction and the implementation of a new drop size distribution model. The most significant change to the TMI V7 ocean algorithm is the addition of a probability of precipitation parameter. Pixels are no longer screened as raining or nonraining before the Bayesian scheme is applied. As a result, many pixels that were previously classified as nonraining in V6 are now assigned a percent probability of rain with a nonzero raining rate in V7. The algorithm documentation recommends using a 50% probability of rain threshold in the field of view when comparing instantaneous PR and TMI rain rates [National Aeronautics and Space Administration Goddard Space Flight Center (NASA GFSC) 2012]. Over land, pixels are still screened as raining or nonraining. The only change to the TMI coastal algorithm is a change in the land–ocean classification (see section 2c). Use of the stage-IV reference (discussed in section 2a) in this study allows for independent evaluation of all four TRMM algorithms (PR V6, PR V7, TMI V6, and TMI V7).

2. Data

a. Datasets

This study utilizes satellite data from TRMM and ground-based radar data from the Next Generation

Weather Radar (NEXRAD) Multisensor Precipitation Estimates (MPE) product (Fulton et al. 1998; Fulton 2002). The multisensor radar estimates are derived from a combination of Weather Surveillance Radar-1988 Doppler (WSR-88D) precipitation estimates (Fulton et al. 1998) and real-time surface rain gauge observations from the Hydrometeorological Automated Data System. Specifically, this study uses the stage-IV dataset, which is a mosaicked national product available from the National Centers for Environmental Prediction (NCEP). The stage-IV data are convenient because they combine precipitation data from the regional forecasting centers into a single product available in an hourly format. A major advantage of the stage-IV dataset is that it covers a larger geographical area than the TRMM GV program (Wolff et al. 2005). Previous studies have identified various biases within the stage-IV dataset. By comparing two stage-IV pixels with rain gauges at an hourly time scale, Habib et al. (2009b) found a conditional bias, with overestimation at rain rates less than $0.5 \, \mathrm{mm \, h^{-1}}$ and underestimation at rain rates greater than $10 \, \mathrm{mm \, h^{-1}}$. The stage-IV hourly estimates correlate well with surface rain gauges (0.8–0.9), with more scatter and lower correlations at light rain rates. The main concern for this study is the high event scale bias, which was found to reach up to ±25% of the event total rainfall in half of events.

The stage-IV data are compared with two TRMM rainfall algorithms, the PR 2A25 algorithm (Iguchi et al. 2000) and the TMI 2A12 algorithm (Kummerow et al. 1996, 1998). The TRMM data source is the Tropical Cyclone Precipitation Feature (TCPF) database (Jiang et al. 2011). The TCPF database includes global TC best-track information, collocated PR and TMI measurements and retrievals, and environmental parameters derived from NCEP reanalysis. Versions 6 and 7 of the algorithms are used, resulting in a total of four TRMM rainfall estimates for each overpass. Only data within the PR swath are considered, which has a 247-km width for the period of interest (after 2001 orbital boost). The TRMM and stage-IV dataset are both available for the 2002–10 Atlantic Ocean hurricane seasons. The PR has a minimum reflectivity threshold of 17–18 dBZ, which limits its ability to resolve rain rates below 0.2–$0.4 \, \mathrm{mm \, h^{-1}}$. The TMI 2A12 estimates rain rates as low as $0.1 \, \mathrm{mm \, h^{-1}}$ but has limited ability to accurately detect warm rainfall over land. As a result, any comparison between the estimates has lowest confidence at the lightest rain rates.

b. Data selection

A semiautomatic matching algorithm is applied to find TRMM overpasses within range of ground-based radar data. First, overpasses of interest are identified by comparing the latitude and longitude coordinates of the best-track TC center with the latitude–longitude of WSR-88D locations in the southeastern United States. Second, the overpasses are manually filtered to remove storms where the PR swath is too far from the coast and storms where a negligible amount of TC-related raining features are within range of the ground-based radars. The subjective criteria in this step are relatively loose: overpasses are accepted if any TC-related precipitation area is identified within TRMM and radar range. The total of 252 overpasses include some cases where the TC center is not necessarily located right along the coast, as the outer bands in large TCs can extend up to 500 km or more from the TC center. Since the PR swath does not cover the entire storm, all overpasses are only representative of a small portion of the TC, mostly the outer bands. The other subjective step in the data selection process is determining the cutoff between TC- and non-TC-related rain features. A rectangular box is manually drawn around each swath to designate the area around all TC-related precipitation within the PR swath.

After the data are selected, the pixel-level algorithm datasets are averaged to a common resolution. The grid averaging process must be considered carefully, since any change to the algorithms' native resolution will introduce additional random errors into the comparisons. The stage-IV, PR 2A25, and TMI 2A12 datasets all have different resolutions. The stage-IV resolution is 4 km × 4 km, the PR 2A25 is 5 km × 5 km, and the TMI 2A12 is about 5.5 km × 12 km. The TMI 2A12 dataset has the lowest resolution and therefore limits the resolution of the grid for comparison. The TMI 2A12 is aligned so the 5.5 km side is across swath (perpendicular to the satellite motion) and the 12 km side is along swath. However, observations from the lower-resolution 10-, 19-, and 37-GHz channels are included in the TMI 2A12 algorithm, so the effective field of view is much larger than the footprint. This study uses relatively small grid boxes with a 1/7° by 1/7° resolution, which equates to about 16 km latitude by 13 km longitude. All pixel-level observations are averaged into each grid-based rain rate. The probability of rain was not considered when selecting TMI V7 pixels over ocean, although the parameter is discussed separately in section 3g.

The temporal resolution of the different datasets must also be considered in the matching process. The TRMM data are instantaneous rain rates (mm h^{-1}), while the stage-IV dataset is an hourly rainfall accumulation (mm) based primarily on the aggregate precipitation estimates from all individual WSR-88D volume scans within that hour period. Although it is possible to choose the individual radar scan closest to the TRMM overpass time,
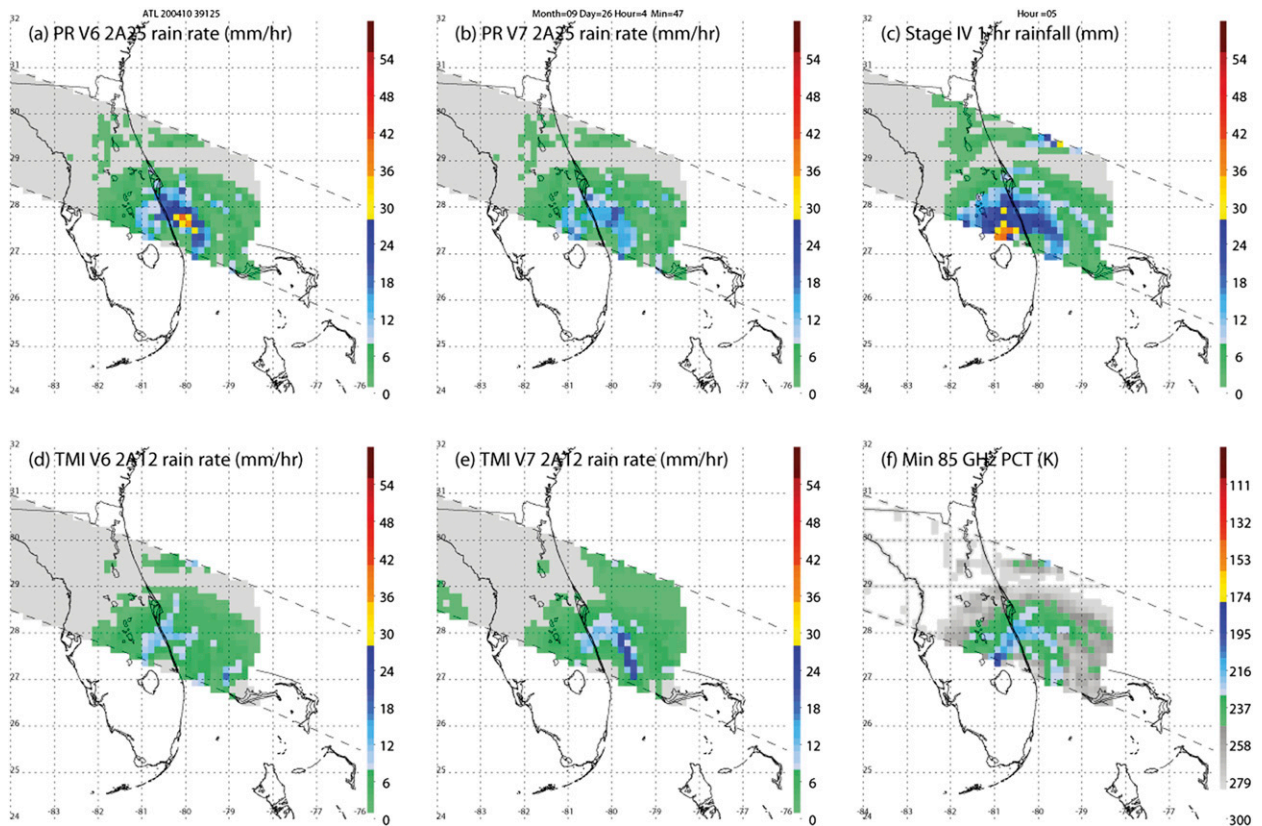
FIG. 1. Example plot of a TRMM overpass from 2004 Hurricane Jeanne compared with the stage-IV 1-h rainfall. The TRMM overpass occurred at 0447 UTC and the stage-IV rainfall is a total accumulation from 0400 to 0500 UTC. All data are averaged to a matching 1/7° grid. The algorithms are (a) PR 2A25 V6, (b) PR 2A25 V7, (c) stage IV, (d) TMI 2A12 V6, (e) TMI 2A12 V7, and (f) TMI minimum 85-GHz PCT.

the raw radar data can experience errors from radar calibration, anomalous propagation, brightband enhancement, radar beam blockage, nonuniform vertical package of reflectivity, and uncertain microphysical parameters such as the reflectivity–rainfall Z–R coefficients (e.g., Smith et al. 1996; Nelson et al. 2010; Breidenbach and Bradberry 2001). Raw radar rainfall estimates do not benefit from the mosaicking, bias corrections, and rain gauge data in the stage-IV dataset. The main additional source of error from the stage-IV data is the change in rain rate as the precipitation evolves and propagates over an hourly period. The errors should be at their lowest when the TRMM overpass occurs around 30 min past the hour and when the bands within the TC are relatively stationary. If the TRMM overpass is within 10 min of an hour, the two closest stage-IV estimates are averaged together. For convenience, this study often refers to the stage-IV data in units of rain rate (mm h^{-1}), even though it is actually a 1-h accumulation.

An example of the averaged data is shown in Fig. 1. Hurricane Jeanne (2004) was captured by TRMM at 0447 UTC 26 September 2004. The 1-h stage-IV

estimate from 0400 to 0500 UTC is used as the reference dataset. The TMI 85-GHz polarization-corrected brightness temperature (PCT; Spencer et al. 1989) is included for reference in Fig. 1f. The 85-GHz PCT is adjusted to the same grid scale by taking the lowest brightness temperature value within each grid box. In Figs. 1a–e, the gray boxes represent accepted data points with zero rain. A qualitative comparison between the TRMM algorithms and stage-IV dataset reveals that the eye, inner core, and rainbands line up fairly well between the different estimates at the pixel level. The location of the heaviest rain is different in each image. The stage IV has the heaviest rain totals (>35 mm h^{-1}) over land, while the PR has the highest rates over ocean. Versions 6 and 7 of the PR show surprisingly large differences, although in most other cases they are in much closer agreement than this example. The center is correctly located by the TMI algorithms, but the banding structures are not as well defined. Another error source is visible over ocean in the TMI V7, as the TMI V7 detects rain everywhere to the northeast of the center, while all the other algorithms have a rain-free area
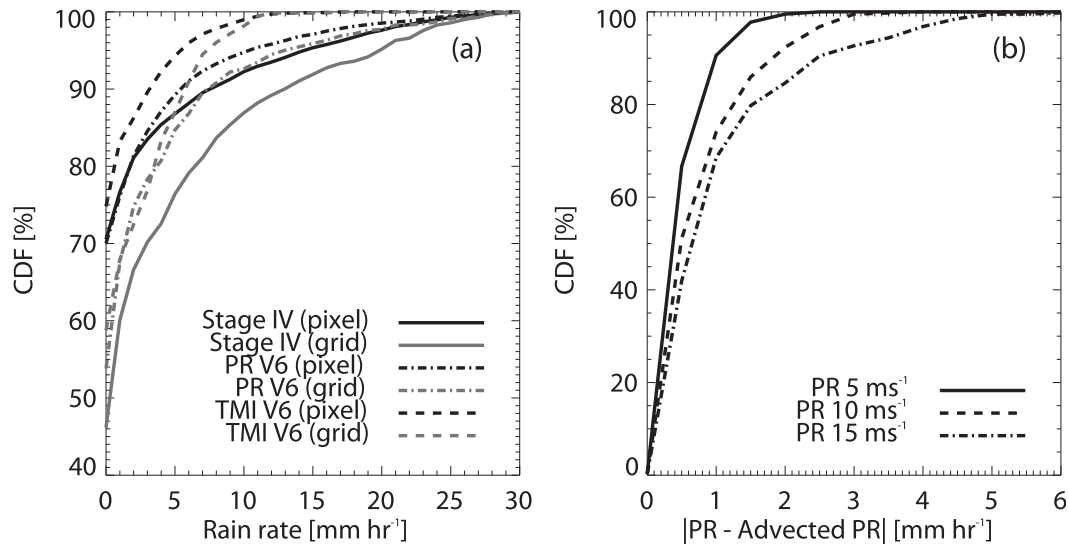
FIG. 2. (a) CDF of the pixel-level rain rates (black lines) and the grid-averaged rain rates (gray lines) for the stage-IV, PR V6, and TMI V6 rain rates. (b) CDF of the absolute difference between the grid-averaged PR V6 rain rates compared with the 1-h-averaged PR V6 rain rates after being advected zonally at 5, 10, and $15\,\mathrm{m\,s^{-1}}$. Both panels exclusively use data from the TRMM orbit 39125 in Fig. 1.

between the bands. This discrepancy is seen on almost all TMI overpasses over ocean and arises as a result of the TMI V7 probability of rain parameter.

c. Spatial and temporal averaging

The differences introduced by the spatial and temporal grid averaging are estimated by comparing the raw pixel-level rain rates to the gridded data from the example overpass in Fig. 1. Figure 2a shows the cumulative data functions (CDF) distribution of the raw pixel-level data compared with the grid-averaged rain rates. The main difference caused by decreasing the resolution with grid averaging is an increase in the raining area from nonraining rain pixels that get averaged with raining pixels. Grid averaging increases the stage IV by 20%–25% and the PR and TMI areas with rain by 15%–20% relative to pixel-level areas with rain. Bins with light rain rates are also affected, but the dominant difference between the distributions at rain rates greater than zero is caused by the algorithms themselves and not the grid averaging. The CDFs are shifted to the right and converge at moderate to high rain rates.

The difference caused by precipitation advecting over the hourly MPE period can also be roughly estimated. The PR V6 overpass in Fig. 1 is hypothetically advected at a constant zonal velocity of 5, 10, and $15\,\mathrm{m\,s^{-1}}$ using 1-min time steps over a 1-h period. Figure 2b displays CDFs of the absolute difference between the conditional (>0) grid-averaged PR V6 rain rates and the same rain rates averaged over the 1-h period after being

advected. The average absolute difference between the original and advected orbits is 0.8, 1.4, and $1.9\,\mathrm{mm\,h^{-1}}$ for the respective 5, 10, and $15\,\mathrm{m\,s^{-1}}$ advection speeds. For the 252 storms in this study, the average storm center speed is $5.3\,\mathrm{m\,s^{-1}}$ and only 15 storms are moving faster than $10\,\mathrm{m\,s^{-1}}$. However, individual bands and storm cells also evolve relative to the storm center, so the actual difference between the instantaneous and hourly averaged PR rain rates is likely between the 5 and $10\,\mathrm{m\,s^{-1}}$ distributions. Figure 2 illustrates that the overall rain-rate distributions should accurately reflect the algorithms themselves, although caution is required when comparing individual grid boxes directly.

d. Final dataset

The final dataset is divided into land, ocean, and coastal/mixed components using the TMI surface flag. The surface flag is stored at the TMI 2A12 resolution, so some of the lower-resolution grid boxes inevitably have two types of surface flags. To resolve this issue, grid boxes with less than two-thirds ocean or land surface flags were added to the coast/mixed category. Some of the surface flag definitions changed between V6 and V7, resulting in a different number of grid boxes for each surface category for the two algorithm versions. A graphical representation of the final dataset is displayed in Fig. 3. The red colored coast/mixed category extends farther out to sea and covers only large inland lakes in V7. Grid boxes where all three version 6 or 7 estimates (PR, TMI, and stage IV) agree on a zero rain rate are removed from
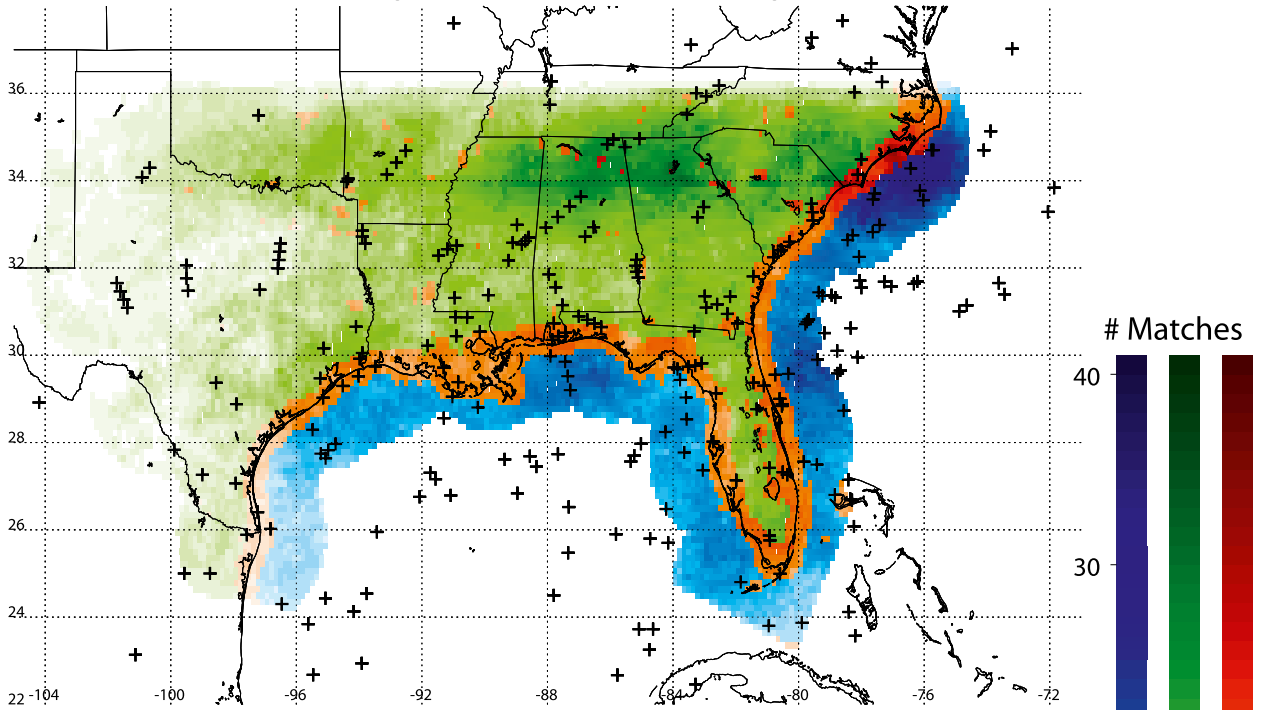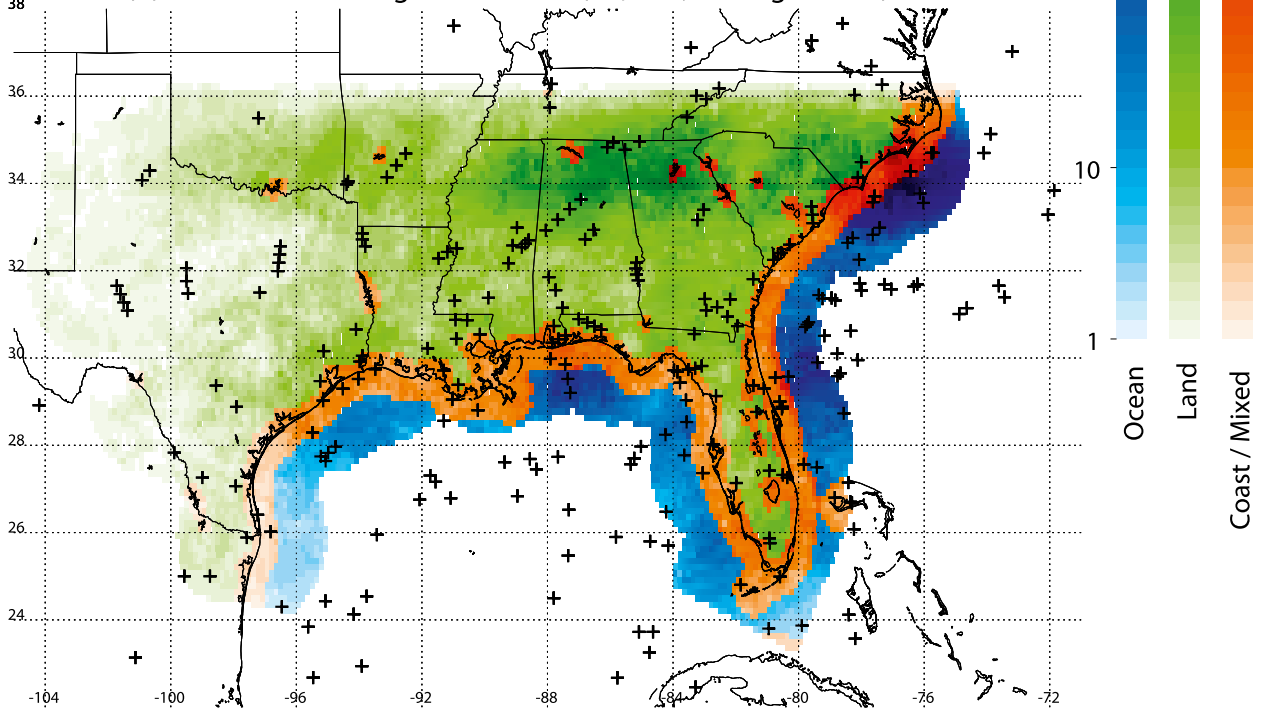
FIG. 3. Geographical distribution of 1/7° grid boxes color coded by TMI surface flag. Darker shades indicated higher data coverage. Grid boxes where the PR, TMI, and stage IV all estimate zero rain are not included in this figure.

the dataset, leaving only the matches where at least one estimate has a nonzero rain rate. As a result, a total of 210 741 grid boxes are reduced to 116 025 for V6 and 120 447 for V7. The color shading in Fig. 3 represents the number of times that each grid box is included for a storm in the dataset. In V6, the dataset is 25% ocean, 58% land, and 17% coast/mixed. In V7, the different surface flags change the distribution to 22% ocean, 56% land, and 21% coast/mixed. It is unlikely that the change in surface flag designations has a quantifiable effect on the results of this study.

The spatial range of the dataset cuts off to the north at the apex of the TRMM orbit, 35°N. Over ocean, the cutoff is 230 km from the nearest WSR-88D location. The stage-IV grids that are located over ocean do not benefit from gauge validation and likely suffers from range degradation associated with beam overshoot and partial beam filling (Breidenbach and Bradberry 2001). Using seasonal WSR-88D rainfall estimates in Oklahoma, Smith et al. (1996) found that warm-season underestimations are most pronounced beyond 150 km and the problem is primarily caused by lack of detection. The stage-IV dataset might be missing some shallow precipitation over the oceanic range, although deeper, convective rainfall should be detected. However, the results from this study suggest that stage IV actually has greater rain coverage over ocean than the PR. Near the Florida Straits, the stage-IV data range cuts off within 230 km of the Key West and Miami radars, so the edge of the dataset takes on a square appearance in that area. The number of observations varies geographically because of both the climatological storm tracks and the TRMM orbital geometry. The North Carolina coast has the most observations, including 9 from one storm: 2005 Hurricane Ophelia. Another maximum occurs around the northern coast of Florida, which saw several slow-moving storms in 2004. Farther south, the TRMM orbital track makes PR swath more likely to miss the storm, resulting in a smaller number of observations.

Figure 3 also designates the location of the TC centers at the time of the TRMM overpasses using + signs. Most of the TC centers are located within about 250 km of the coastline, but a few are located well inland and others are 500 km or more from the coast. Some of the points from the same storm are clustered together, indicating that the storm was seen by TRMM on consecutive orbits. Large, slow-moving storms north of 30° latitude were observed by as many as four overpasses in a row, with each overpass coming about 90 min apart. In terms of TC intensity, the dataset includes 94 tropical depressions, 104 tropical storms, 40 category 1–2 hurricanes, and 15 category 3–5 hurricanes. Many of the tropical storms and depressions were originally landfalling hurricanes that still had a

much larger and more intense rain field than an average storm of that intensity. Because there are 252 overpasses included, any local or storm-specific biases should not factor strongly into the overall results. No regional biases were detected.

3. Statistical methods

Several statistical methods are utilized to compare the algorithms. Mean rain rates (conditional and unconditional) are computed to determine the overall rainfall magnitudes. The unconditional rain rate is calculated as the average of all grid boxes, including those that are raining and nonraining. The conditional rain rate includes only the raining, or nonzero, grid points from each individual algorithm. The conditional rain rate has a different sample size for each algorithm depending on how often it assigns nonzero rain rates. The percentage of pixels with rain rates > 0, 1, 5, and 10 mm h^{-1} are provided to aid in the comparison. Other commonly used statistics in this study include the use of PDFs, scatterplots, and Pearson's correlation coefficient.

a. Bias decomposition

Bias statistics are most useful when each of the four TRMM algorithms is individually evaluated relative to the stage-IV estimates. For example, the PR 2A25 version 6 and stage-IV algorithm can be compared for only the pixels where either of the two algorithms is >0. The individual comparison removes any bias that PR V7 or the TMI algorithms have on the sample selection. From these results, the mean bias is the mean difference in rain rate between the respective TRMM algorithm (R_T) and the stage-IV estimate (R_{IV}):

$$B = \frac{1}{n}\sum(R_T - R_{IV}), \quad (3.1)$$

where n is the sample size where either R_T or R_{IV} is greater than zero. It is also desirable to decompose the mean bias into three components, following the formulas used in Habib et al. (2009a). The hit bias (HB) is defined as the portion of the mean bias contributed from grid points where the TRMM and stage-IV algorithms both agree that the rain is nonzero:

$$HB = \frac{1}{n}\sum[R_T(R_T > 0 \quad \text{and} \quad R_{IV} > 0)$$
$$- R_{IV}(R_T > 0 \quad \text{and} \quad R_{IV} > 0)]. \quad (3.2)$$

The missed rain bias (MB) is the portion of the mean bias contributed from grid points where the TRMM

rain rate is equal to zero and the stage-IV rain rate is nonzero:

$$MB = \frac{1}{n}\sum R_{IV}(R_T = 0 \quad \text{and} \quad R_{IV} > 0). \quad (3.3)$$

More simply put, the missed rain bias is computed where the TRMM algorithm estimated zero rain in a grid box where rain was detected by stage IV. Finally, the false rain bias (FB) is the portion of the mean bias contributed from grid points where the TRMM rain rate is nonzero and the stage-IV rain rate is equal to zero, or where the TRMM algorithm falsely estimated nonzero rain:

$$FB = \frac{1}{n}\sum R_{TRMM}(R_{TRMM} > 0 \quad \text{and} \quad R_{IV} = 0). \quad (3.4)$$

The three components of bias add up to the mean bias. The bias decomposition is most useful for determining the percentage of the total bias that can be attributed to detection issues (i.e., missed and false bias) relative to the rain-rate magnitude (hit bias).

b. Mean error decomposition

The root-mean-square error (RMSE) is a commonly used statistic that is applied in this study to compute the average difference between the TRMM algorithms and the stage-IV reference dataset. Using simple linear regression, the RMSE can also be decomposed to provide insight on what fraction of the difference between the PR/TMI and stage IV can be attributed to systematic ($RMSE_s$) and random ($RMSE_r$) errors, which add up to the total RMSE:

$$RMSE = RMSE_s + RMSE_r = \sqrt{\frac{1}{n}\sum (R_T - R_{IV})^2}. \quad (3.5)$$

From Willmott (1982), the systematic RMSE is defined as

$$RMSE_s = \sqrt{\frac{1}{n}\sum (R_T' - R_{IV})^2}, \quad (3.6)$$

and the random RMSE is

$$RMSE_r = \sqrt{\frac{1}{n}\sum (R_T - R_T')^2}. \quad (3.7)$$

In the above equations, R_T is the rain rate for a TRMM grid box, R_{IV} is the corresponding stage-IV rain rate for the grid box, and R_T' is the TRMM rain rate predicted by least squares regression of the TRMM rain rates,

$$R_T' = a + b \times R_{IV}. \quad (3.8)$$

In other words, the systematic error is the mean squared difference between the predicted TRMM distribution and the stage-IV estimate. The random error is the mean squared difference between the TRMM estimate and the predicted TRMM distribution. The percentage of the MSE that is attributed to systematic error is simply $RMSE_s/RMSE$. These statistics were originally used to evaluate model performance (Willmott 1982; Willmott et al. 1985) although they have more recently been used in Habib et al. (2009a,b) to compare stage-IV data with TRMM and rain gauge observations. One addendum with this decomposition method is that the stage-IV dataset is assumed to be correct. It is not possible to determine if the systematic error can be attributed to the TRMM or stage-IV dataset, just that there are systematic differences between them. However, the relative difference in systematic error between the PR and TMI datasets compared with the same stage-IV reference does give information about how much systematic error can be attributed to each TRMM algorithm.

4. Results

a. Mean values

The mean values from the combined dataset of 252 storms are displayed in Table 1. The leftmost section displays the number of grid boxes, which is separate for V6 and V7 because of the difference in land, ocean, and coastal surface designations. Consequently, the stage-IV rain rates are calculated independently using the different surface flags in V6 and V7. Unlike most other statistics in this study, these sample sizes add up to the total sample of around 210 000 grid boxes that includes zero rain boxes. The mean rain rates are easiest to interpret by comparing with Table 2, which displays the percentage of all grid boxes with rain rates > 0, 1, 5, and 10 mm h^{-1} for each algorithm.

Over ocean, the unconditional mean rain rates are all within about 10% of each other. In V6, the PR and TMI have lower unconditional rain rates and greater conditional rain rates than the stage-IV reference. By comparing to Table 2, it is apparent that this discrepancy is caused by the stage IV detecting 8%–9% more nonzero grid boxes than the TRMM algorithms. The TMI has the highest conditional rain rate out of the V6 ocean algorithms because of a combination of fewer raining grid boxes and a greater contribution from grid boxes with rain rates > 5 mm h^{-1}. The number of PR V7 raining grid boxes increase slightly at all rain-rate criteria relative to V6, including an 11% increase in the percent of

TABLE 1. Sample size of all grid boxes including zero rain rates, unconditional mean rain rate (including all grid boxes) and conditional mean rain rate (including only grid boxes with nonzero rain rates).

Algorithm	No. grid boxes ≥ 0			Unconditional mean rain rate			Conditional mean rain rate		
	Ocean	Land	Coast/mix	Ocean	Land	Coast	Ocean	Land	Coast
Stage IV (V6)	47 426	126 446	36 869	1.33	1.07	1.27	2.52	2.20	2.60
PR V6				1.25	0.83	0.98	2.79	2.21	2.57
TMI V6				1.28	0.83	0.83	2.90	2.73	3.05
Stage IV (V7)	34 590	128 356	47 620	1.37	1.07	1.26	2.55	2.21	2.54
PR V7				1.34	0.85	1.06	2.95	2.31	2.74
TMI V7				1.44	0.65	0.81	1.89	2.16	3.05

grid boxes with rain rates greater than 5 and 10 mm h^{-1} relative to V6. It is somewhat surprising that the stage-IV dataset finds more areas of light rain than the PR in both V6 and V7 because the oceanic dataset is almost completely located between 100 and 230 km from the nearest ground-based radar site. It is expected that some shallow and/or stratiform precipitation would be underneath the lowest elevation radar scan. However, the PR does have a 17–18-dBZ minimum detection threshold, so it is possible that both datasets are missing some very light precipitation. The TMI V7 has over a 30% increase in grid boxes > 0 relative to V6, a consequence of the probability-of-rain parameter (see section 4g).

The mean rain rates over land are generally much lower than over ocean. Based on the unconditional rain rate, the PR and TMI V6 appear to agree almost exactly, but the distribution of rain rates in Table 2 suggests that the TMI V6 is assigning zero rain to some of the grid boxes with PR V6 and stage-IV rain rates between 0 and 1 mm h^{-1}. Light rainfall is notoriously difficult to detect over land, although it appears that rain rates > 1 mm h^{-1} are mostly being detected successfully. When the criteria rise to >1 mm h^{-1}, TMI V6 is more closely in line with stage IV than the PR. In V7, the percentage of grid boxes > 0 remains almost exactly the same relative to V6, but the TMI V7 mean rain rates are considerably lower than V6. The TMI V7 land algorithm finds fewer grid boxes in the >1 and >5 mm h^{-1} rain-rate ranges. All of the TRMM land algorithms find a significantly smaller percentage of raining grid boxes over land relative

to over ocean. The stage-IV reference is also lower over land, but by a much lower margin. Lower raining coverage and rain rate over land relative to ocean is reasonable, since TCs are weaker after landfall, but it is likely that the decrease between land and ocean in the PR and especially the TMI is too steep. The mean rain rates over coastal areas are generally in between the ocean and land values. Figure 3 shows that the majority of coast/mixed pixels are over coastal oceanic areas, so it is not surprising that the stage-IV unconditional rain rates are closer to the oceanic estimate. However, in both V6 and V7, the PR detects about 10% fewer grid boxes > 0 than the stage IV, which is similar to what is observed over land. The coast/mixed mean rain rates do not change much between V6 and V7 because the TMI coastal algorithm was not updated in V7 (NASA GFSC 2012).

b. Contributions to mean rain rate

The mean rain-rate analysis is a good starting point, but it is incomplete without additional information about the distribution of rain rates and their relative contributions to the mean rain rate. From Table 2, about half of the nonzero grid boxes have a rain rate less than 1 mm h^{-1} and only around 6%–8% have a rain rate greater than 5 mm h^{-1}. Although the higher rain rates make up just a small portion of the sample, they have a disproportionately large influence on the mean rain rates and hence the disagreements between the algorithms. Figures 4 and 5 both show the contribution to the

TABLE 2. Percentage of all grid boxes with rain rates > 0, 1, 5, and 10, divided by algorithm and surface flag.

| Algorithm	% grid boxes > 0 (%)			% grid boxes > 1 (%)			% grid boxes > 5 (%)			% grid boxes > 10 (%)		
	Ocean	Land	Coast	Ocean	Land	Coast	Ocean	Land	Coast	Ocean	Land	Coast
Stage IV (V6)	52.8	48.7	48.8	26.4	22.8	22.7	7.8	6.3	7.5	2.7	2.0	3.0
PR V6	44.6	37.6	38.2	23.0	18.6	19.2	7.0	4.8	5.6	2.7	1.1	1.9
TMI V6	44.1	30.4	27.3	25.2	24.1	20.0	8.6	3.4	4.7	2.5	0.8	1.0
Stage IV (V7)	53.5	48.5	49.8	26.9	22.1	23.6	8.0	6.3	7.5	2.8	2.0	2.8
PR V7	45.4	36.8	38.6	24.1	18.7	20.1	7.8	4.6	6.2	3.0	1.3	2.2
TMI V7	75.8	30.0	26.6	27.7	19.6	19.3	7.8	1.9	4.6	2.6	0.7	0.9
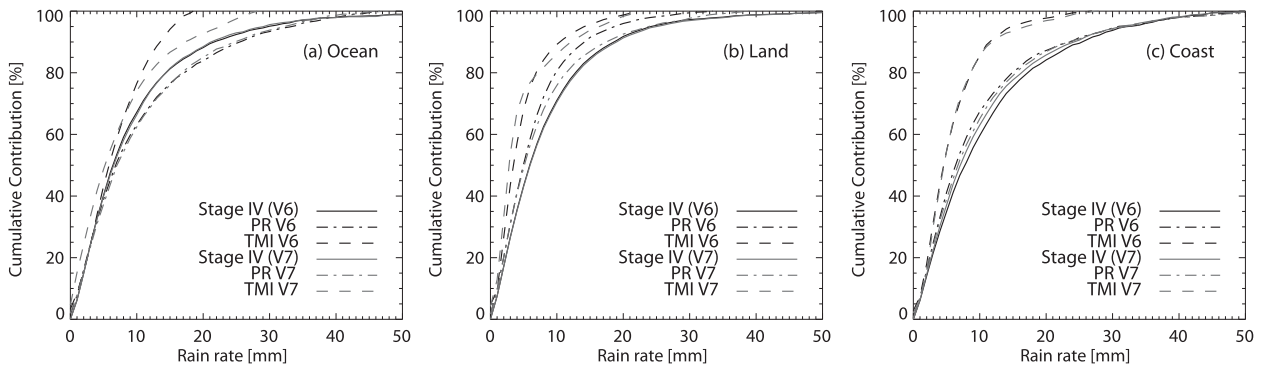
FIG. 4. Cumulative contribution (%) to mean rain rate for TRMM algorithms compared with the stage-IV reference dataset, divided by (a) ocean, (b) land, and (c) coast/mixed surface.

mean rain rate from all of the individual rain rates in 1 mm h^{-1} bins. Compared with a traditional CDF plot, the cumulative contribution is better distributed across the full range of rain rates. The oceanic plot (Fig. 4a) reveals that about 60% of the mean rain rate is derived from grid boxes with rain rates below 10 mm h^{-1}. The TMI V7 ocean algorithm derives the most rainfall from light rain rates, the rest of the ocean algorithms agree at <5 mm h^{-1} rates and diverge in the 5–10 mm h^{-1} range. Version 7 of the TMI is clearly improved relative to V6 at higher rain rates. However, TMI V7 is still not getting enough contribution from >10 mm h^{-1} rain rates. This plotting method does not pick up much difference between PR V6 and V7 over ocean, although both have slightly less contribution to the mean than stage IV starting around 5 mm h^{-1} and up. The numerical contribution to mean rain rate in Fig. 5 shows the same data as Fig. 4 but emphasizes the rain-rate ranges that contribute the most to the mean. It is interesting that TMI V6 has more contribution from 5–15 mm h^{-1} rain rates than the PR, which is consistent with other studies of TMI V6 over ocean in tropical cyclones (Cecil and Wingo 2009; Zagrodnik and Jiang 2013). It appears likely that

TMI V6 is identifying the areas of moderate rain, but assigning rain rates of 5–15 mm h^{-1} to a number of pixels that should have rain rates of 15–30 mm h^{-1} or higher.

The cumulative contribution over land (Fig. 4b) has a stage-IV curve that looks about the same as the oceanic curve, but noticeably different PR and TMI distributions. There is a major difference between the stage IV and TMI at light rain rates. The TMI algorithms derive about 80% of their mean rain rates from <5 mm h^{-1} rain rates, but the stage IV only finds about 50% of the mean rain rate comes from the <5 mm h^{-1} bins. The stage-IV estimate suggests that about 10% of the mean should come from rain rates above 20 mm h^{-1}; however, both TMI algorithms also get essentially zero contribution from the heavy rain rates. The PR curves show some difference over land, with PR V7 coming much closer to stage IV above 5 mm h^{-1} and especially above 15 mm h^{-1}. Figure 5 suggests that the TMI needs to have less contribution from the 3–6 mm h^{-1} rain rates and more in the 7–20 mm h^{-1} range. The coastal plots are similar to the land plots. The PR is closer to the stage-IV reference and the most significant area of TMI underestimation is higher than over land, in the 10–30 mm h^{-1} range.
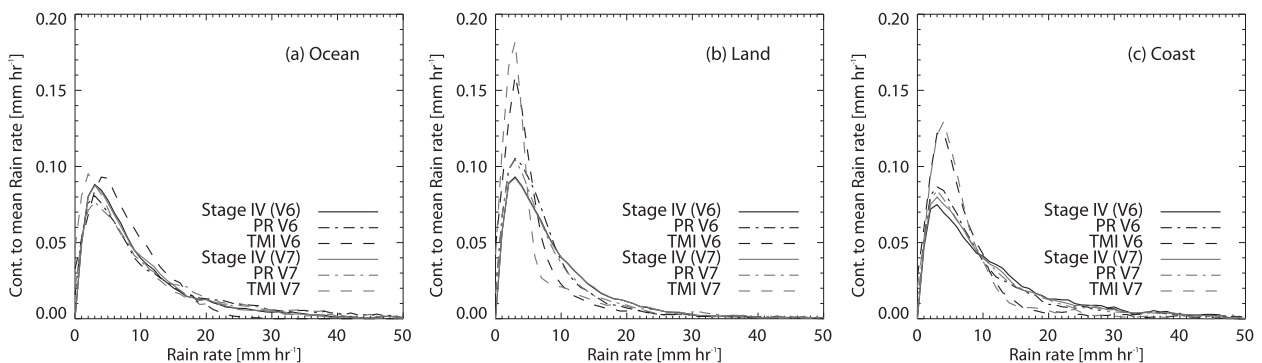

FIG. 5. Contribution to mean rain rate for TRMM algorithms compared with the stage-IV reference, divided by (a) ocean, (b) land, and (c) coast/mixed surface. Data are divided into bins of 1 mm h^{-1}.
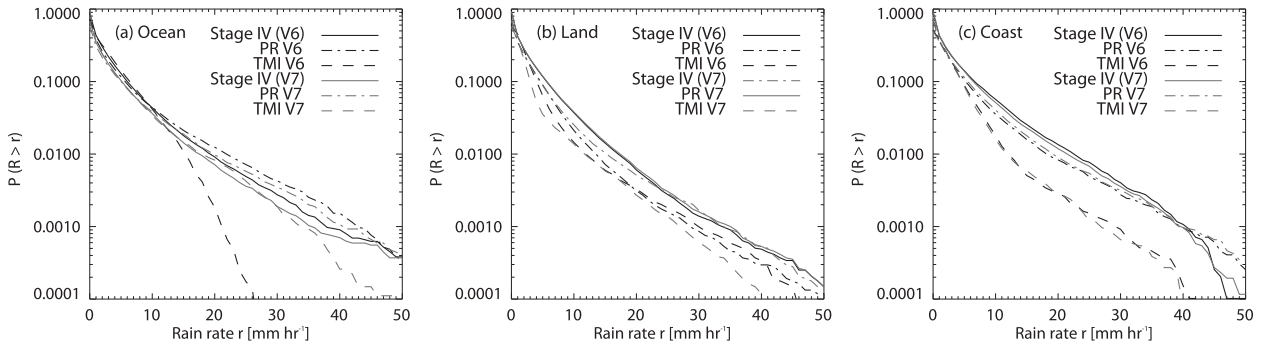
FIG. 6. Probability of exceedance plots for TRMM algorithms compared with the stage-IV reference dataset, divided by (a) ocean, (b) land, and (c) coast/mixed surface.

c. Probability distributions

The probability distributions look at the difference in rain rates without considering the contribution to the mean. In Fig. 6, the probability of exceedance function is calculated for each algorithm. The probability of exceedance is the probability that the rain rate in a given grid box (R) exceeds a certain threshold (r). A logarithmic plot is used on the y axis because the relative frequency of high rain rates is rare. Figure 6a shows that only around 5% of oceanic grid boxes have rain rates exceeding $10 \, \mathrm{mm \, h^{-1}}$. The cumulative contribution (Fig. 4a) demonstrates that these $>10 \, \mathrm{mm \, h^{-1}}$ boxes account for about 40% of the cumulative rainfall. Over ocean, the TRMM algorithms find about the same number of grid boxes as stage IV up to about $15 \, \mathrm{mm \, h^{-1}}$. The improvement TMI V7 high rain rates over ocean is limited to rain rates below $35 \, \mathrm{mm \, h^{-1}}$. Both PR V6 and V7 have a higher probability of rain rates exceeding $20 \, \mathrm{mm \, h^{-1}}$ than the stage-IV dataset. The discrepancy at high rain rates is reflected in the high PR conditional mean rain rates in Table 1.

The TMI land algorithms have a lower probability of exceedance than stage IV starting at rain rates of $5 \, \mathrm{mm \, h^{-1}}$ and up. The large difference in the 5–$10 \, \mathrm{mm \, h^{-1}}$ range is emphasized in Fig. 5 because there are a large number of grid boxes in this range. The TMI V6 distribution is overall much closer to stage IV than TMI V7. The PR V7 probability of exceedance curve almost exactly matches stage IV above $20 \, \mathrm{mm \, h^{-1}}$, while PR V6 has less moderate and heavy raining grid boxes. The underestimation of rain over land in V6 has been noted by the algorithm developers and appears to be mostly corrected in V7. The 5–$20 \, \mathrm{mm \, h^{-1}}$ range still is showing some underestimation, but it is improved relative to V6. Figures 4–6 all demonstrate that version 7 of the PR is easily the best-performing TRMM algorithm over land at higher rain rates. Over coasts, the TMI significantly underestimates both moderate and heavy rain rates

relative to stage IV. Above $20 \, \mathrm{mm \, h^{-1}}$, the TMI probability of exceedance is nearly a full order of magnitude too low. The PR coastal algorithm shows fewer grid boxes than stage IV exceeding rain rates of 5–$40 \, \mathrm{mm \, h^{-1}}$. Above $40 \, \mathrm{mm \, h^{-1}}$, the PR, TMI, and stage IV all diverge, although the sample size at these rain rates is too low to have high confidence in that disagreement.

d. Quantile plots

The quantile plots of all individual grid points (Fig. 7) help illustrate the conditional bias between the algorithms. The correlation coefficients (r) are also included to gauge the degree of disagreement. Wang et al. (2009) used a single case study of Hurricane Katrina over land to compare TMI V6 and stage IV and found a correlation coefficient of 0.71 on a 0.25° grid. However, the correlation between TMI V6 and TRMM GV at Melbourne over a 5-yr period is only 0.51, which compares favorably with $r = 0.47$ for the 252 storms in this study. The additional stage-IV raining area relative to the PR (Table 2) results in the PR quantiles favoring stage IV at light rain rates. The PR–stage-IV correlation coefficient is actually lowest over ocean, seemingly a result of PR overestimation at moderate rain rates that is apparent in the probability distributions.

The TMI ocean algorithms have almost as high of a correlation coefficient as the PR and there are no major biases present. The improved agreement in the $>10 \, \mathrm{mm \, h^{-1}}$ range in Fig. 7d relative to Fig. 7c represents a noticeable improvement in the V6 deficiency that was mentioned earlier in Fig. 5. Over land, TMI V6 and V7 show similar biases relative to stage IV. The quantiles are biased toward stage IV at rain rates below $0.5 \, \mathrm{mm \, h^{-1}}$ and rain rates from 5 to $15 \, \mathrm{mm \, h^{-1}}$. Figures 7g and 7h (TMI land) have correlation coefficients below 0.5. The bias at higher rain rates is visibly less in V6 when compared with V7. The TMI coastal algorithm follows the same bias pattern as the TMI land algorithm.
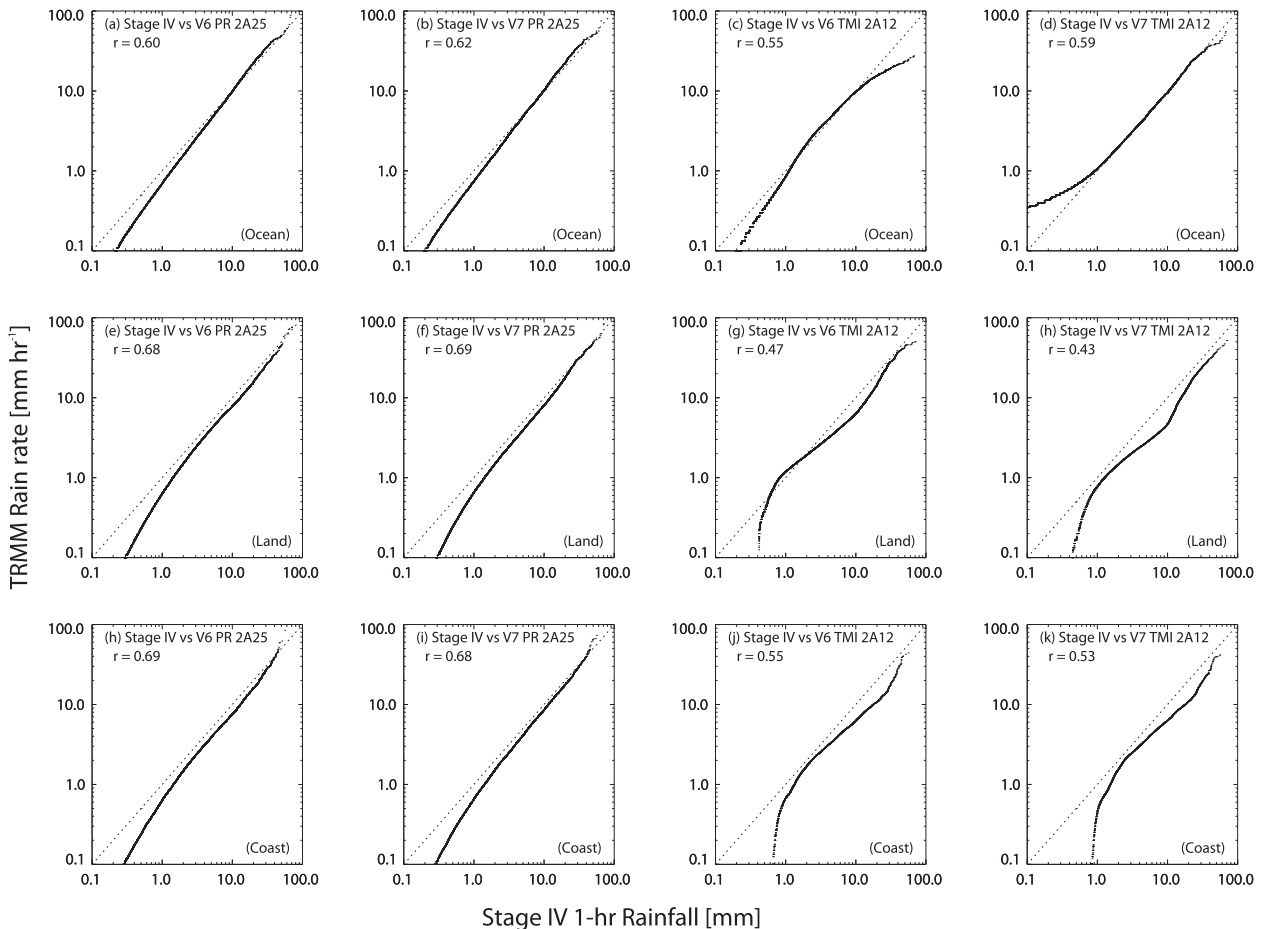
FIG. 7. Scatterplots of stage-IV 1-h rainfall vs TRMM rain rate, divided by TRMM algorithm. The plots are arranged by TRMM algorithm (columns) and land, ocean, and coast/mixed (rows).

e. Error decomposition

With several sources of error in the grid averaging, it is important to quantify how much of the deviation between TRMM and stage IV can be attributed to random versus systematic causes. The error decomposition method described in section 3b is applied to the four TRMM algorithms and the results are displayed in Table 3. The PR always has much lower systematic error than the TMI. Given the spatial and temporal grid resizing in this study, a large amount of random error is expected. The TMI is expected to have more random error from the resizing than the PR because of the discrepancy between the $1/7°$ grid size and the TMI field of view (FOV). If more TMI pixels were added to get an apparent TMI resolution closer to the TMI FOV, the result would be more blending of light and moderate rain rates, which would reduce the rain rate of some of the highest TMI grid boxes. The light and moderate rain rates could change in either direction, since both heavier

and lighter–zero pixels would be averaged in. In other words, the systematic error at moderate to high rain rates (Figs. 7g,h) is likely not caused by the grid resizing. The high percentage of systematic errors in Table 3 is reasonable, although a cautious observer may choose to only consider the relative difference between the V6 and V7 systematic errors.

In any case, it is somewhat surprising that the PR ocean algorithms have a higher RMSE than the TMI algorithms, although some of the difference can probably be attributed to uncertainties in stage IV. The TMI V7 ocean algorithm has both a lower RMSE and 15% less systematic error, representing a major improvement over V6. The improvement above $15\,mm\,h^{-1}$ (Figs. 6 and 7) is the source of the error reduction. About 12% more systematic error still remains compared with PR V7. The systematic error increases for all four algorithms over land relative to ocean. The most striking difference is in the TMI, as V7 has a higher RMSE than V6 and over 10% more systematic error. There is relatively

TABLE 3. Root-mean-square error (RSME; mm h^{-1}) and the percent of the RMSE that can be attributed to systematic biases.

Algorithm	Ocean		Land		Coast	
	RMSE	% system	RMSE	% system	RMSE	% system
PR V6	3.85	13.8	2.75	35.2	3.44	30.7
PR V7	3.85	10.6	2.80	27.0	3.40	22.2
TMI V6	3.60	38.8	3.39	49.5	3.90	62.2
TMI V7	3.31	23.2	3.53	61.4	3.83	61.0

little difference between V6 and V7 over coasts, although the PR systematic error is reduced in V7. The TMI coastal algorithms have a high RMSE, but the large percentage of systematic error suggests that it a bias correction technique may be able to remove a sizable portion of the error.

f. Bias

The bias calculations relative to the stage-IV reference are displayed graphically in Fig. 8. The biases are calculated for each algorithm versus stage IV individually (only grid boxes with either the individual TRMM algorithm or stage IV greater than zero) instead of using the combined dataset. The bias sample sizes are shown in Table 4. The hit bias, miss bias, and false bias add up to the mean bias. The biases for all algorithms are lowest over ocean, with miss bias contributing the most to the mean bias. The oceanic algorithms have a very low hit bias, as rain detection (raining versus non-raining) remains the primary area of uncertainty. All of the land algorithms have a significant negative mean bias, with TMI V7 clearly showing the greatest underestimation. The negative bias in the PR and TMI land algorithms comes from both successful detection and missed detection. Recall that Figs. 4, 5, and 6 show that the PR land underestimation is especially apparent at moderate to high rain rates. Version 7 of the PR does show some improvement over V6 in coastal regions, with less underestimation in raining areas. The systematic error over coasts derives from underestimation from both hits and misses. Finally, it is worth noting that false detection contributes very little to the mean biases as a whole.

The statistical percentages of hits, misses, and false rain are conveyed in Table 4. Both algorithms equaling zero does not count as a hit. The PR has a better hit percentage than the TMI over ocean, with the greatest difference over land and coast. Misses are clearly less frequent over ocean than land, which is expected because the emission-based channels can be added to the ocean algorithm. The TMI has more misses than the PR, especially over coasts. The geographic distribution of

hits, misses, and false rain was also considered. Hits and misses did not show any noteworthy geographic biases. Maps of the false positives are displayed in Fig. 9, normalized for sample size relative to the sample in Fig. 3. Precipitation radar false positives are relatively rare and just above evenly distributed everywhere. In the PR plots (Figs. 9a,b), there is some evidence of false positives caused by the 230-km radar range west of Tampa Bay, but overall the radar range problem does not appear to be significantly affecting the dataset. Version 6 of the TMI has a slightly elevated number of false positives over ocean relative to the PR. Most of the false positives are generated from the TMI V7 algorithm over ocean. The hit percentage is only marginally improved relative to V6, but the number of false positives more than triples to over 30%. The next section examines these false positives in more detail.

g. TMI V7 probability of rain over ocean

The TMI V7 false positives over ocean must be considered in tandem with the TMI probability of rain parameter. Figure 10 examines the pixel-level TMI rain rates and rain probabilities for hits, misses, and false rain as inferred from the gridded data. The criteria are modified slightly from Figs. 8 and 9 to reduce the risk of improper categorization. A hit is defined when all three V7 ocean algorithms are nonzero, a miss is when TMI V7 is zero and *both* stage IV and PR V7 are nonzero. False rain is when TMI V7 is greater than zero and *both* stage IV and PR V7 are zero. The fourth category, all zero, refers to when stage IV, PR, and TMI all agree that the rain rate is zero. This procedure retains 83% of the 34 590 ocean grid boxes including 7136 false TMI V7 grid boxes. Figure 10a shows the CDF of rain rates for the hit and false cases. The leftmost bin contains the zero rain pixels that result from averaging to the larger grid size. The false TMI pixels are mostly 0.5 mm h^{-1} or less. The probability of rain CDF is displayed in Fig. 10b. Only 5% of hits have less than a 100% probability of rain. Misses account for less than 0.5% of all grid boxes and likely result from being in the same grid box as PR and MPE raining pixels. Pixels that are zero in all three algorithms have the lowest probability of rain, generally less than 50%.

The false rain curve has several important characteristics. About one-third of false rain pixels have a 100% probability of rain, while the remaining two thirds are nearly equally spread between 30%–95% probability. Filtering the false TMI V7 pixels with a probability of rain below 50% does little to affect the dataset, especially since most of the <50% false TMI V7 pixels are simply the zero rain pixels that are included from grid averaging. Setting the filter at 90% removes 64% of false pixels while only losing 4% of hits. However, it is difficult
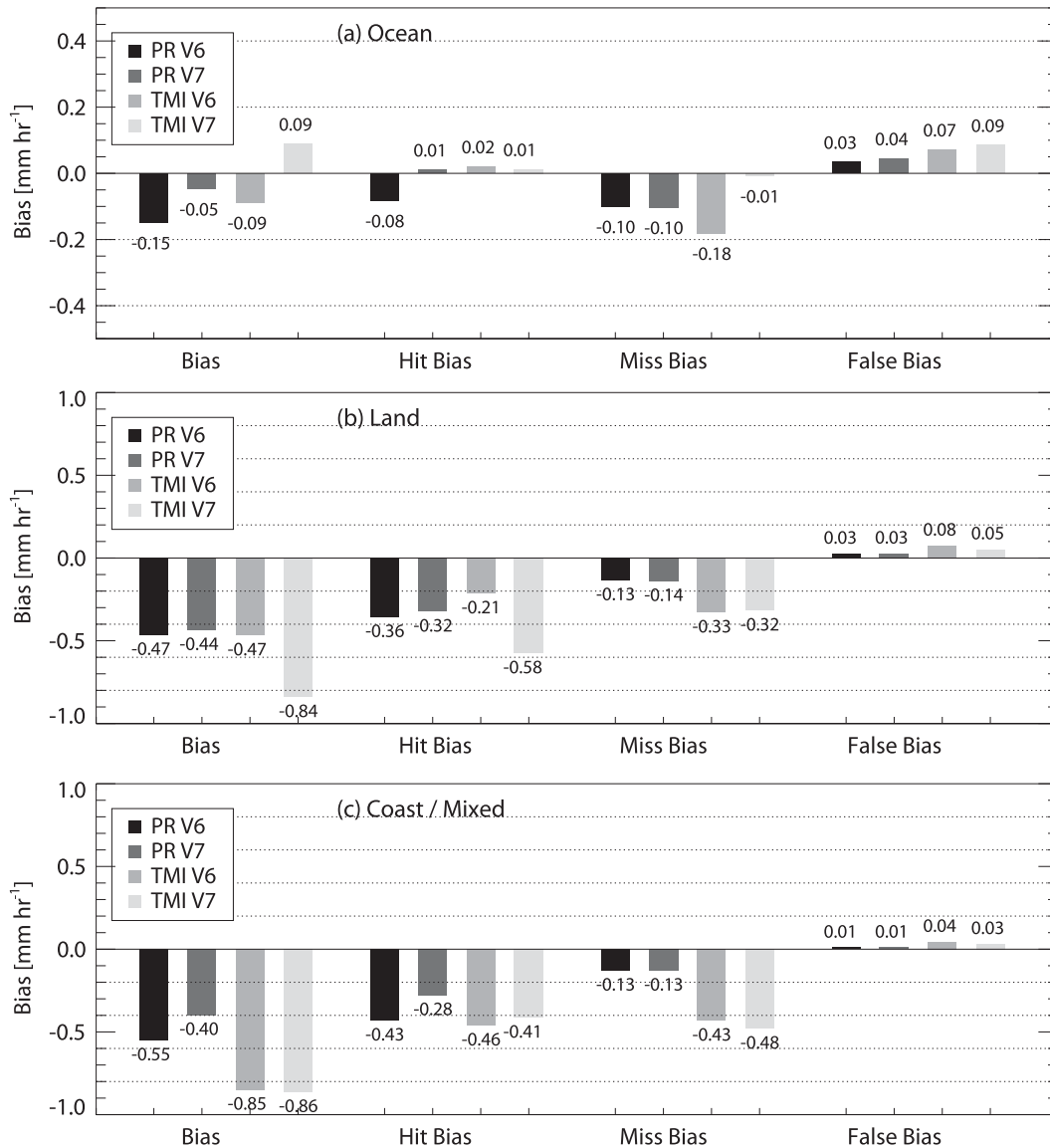
FIG. 8. Bar plots of mean (left to right) bias, hit bias, miss bias, and false bias, divided by (a) ocean, (b) land, and (c) coast/mixed surface.

to determine which filtering criteria are closest to being physically correct. The PR minimum sensitivity is around 0.2–0.4 mm h^{-1} (Schumacher and Houze 2000) and beam overshoot likely limits stage-IV sensitivity over ocean as well. The TMI pixels labeled as "false" with a 100% probability of rain have a mean rain rate of only 0.44 mm h^{-1} and a median of 0.30 mm h^{-1}. Considering these limitations, it is difficult to determine the

TABLE 4. Sample size of grid boxes where each individual TRMM algorithm or the stage-IV reference is nonzero and the percentage of those grid boxes that are designated as hits, misses, or false rain.

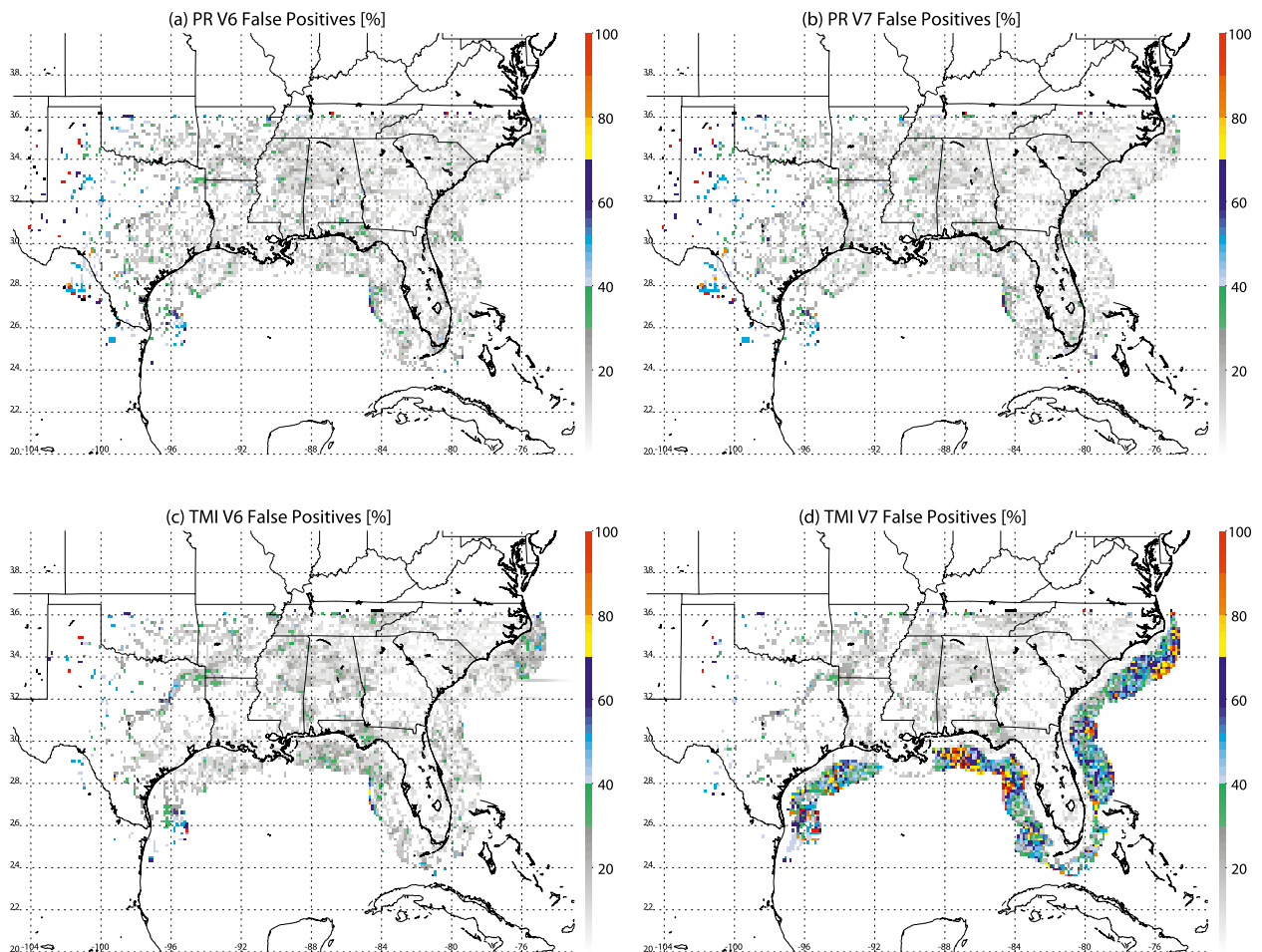| Algorithm	No. grid points			% Hit			% Miss			% False		
	Ocean	Land	Coast	Ocean	Land	Coast	Ocean	Land	Coast	Ocean	Land	Coast
PR V6	26 892	65 787	19 046	72.1	65.9	68.3	21.0	27.7	26.1	6.8	6.4	5.6
PR V7	19 883	66 192	24 906	72.1	65.5	69.0	21.0	28.6	26.3	6.9	5.9	4.7
TMI V6	27 793	65 176	18 878	65.4	53.5	48.5	24.8	41.0	46.8	9.9	5.5	4.8
TMI V7	26 935	65 419	24 901	66.1	54.0	46.2	2.6	41.2	49.1	31.3	4.8	4.7

FIG. 9. Geographic distribution of the percent of grid boxes by location with false positives (TRMM > 0, stage IV = 0), divided by (a) PR V6, (b) PR V7, (c) TMI V6, and (d) TMI V7.

best criteria without additional validation data. There is no clear probability of rain cutoff and no way to distinguish whether TMI V7 ocean pixels with rain rates < $0.5\,mm\,h^{-1}$ are actually false or are just being missed by the PR.

h. Bias relative to 85-GHz ice scattering

Wang et al. (2009) described several known anomalies in the TMI V6 land algorithm, including overestimation in strong, deep convective systems and an underestimation of warm rainfall. A simple way to evaluate these biases using the stage-IV reference is to compare the rain rates relative to the minimum 85-GHz PCT. The threshold for deep convection is generally defined as a system with a minimum 85-GHz PCT < 225 K (Mohr and Zipser 1996). It is difficult to isolate areas of warm rain using only PCT, but generally warm rain will have an 85-GHz PCT around or above 275 K. By using a grid scale, this study also neglects characteristics of the

precipitating systems as a whole that can be better understood using precipitation features (e.g., Mohr and Zipser 1996; Nesbitt et al. 2000; Cecil et al. 2002). Nevertheless, a brief comparison is undertaken to evaluate the TMI–PR relationship as it relates to the 85-GHz ice scattering–rain rate relationship.

Figure 11 displays the mean gridbox rain rate as a function of the minimum 85-GHz PCT and Fig. 12 shows the mean bias. In Figs. 11a and 12a, the ocean algorithms are in almost perfect agreement with stage IV for 85-GHz PCTs above 250 K. Below 250 K, the algorithms have greater disagreements. In the 220–250-K realm, all of the algorithms overestimate stage IV. At lower 85-GHz PCTs, TMI-IV underestimates rain rates and the other three algorithms overestimate. However, the biases are all within about $2\,mm\,h^{-1}$, which is a reasonably acceptable range when considering the high rain rates. Of greater interest is the land algorithm in Figs. 11b and 12b. The TMI overestimation is a strong function of
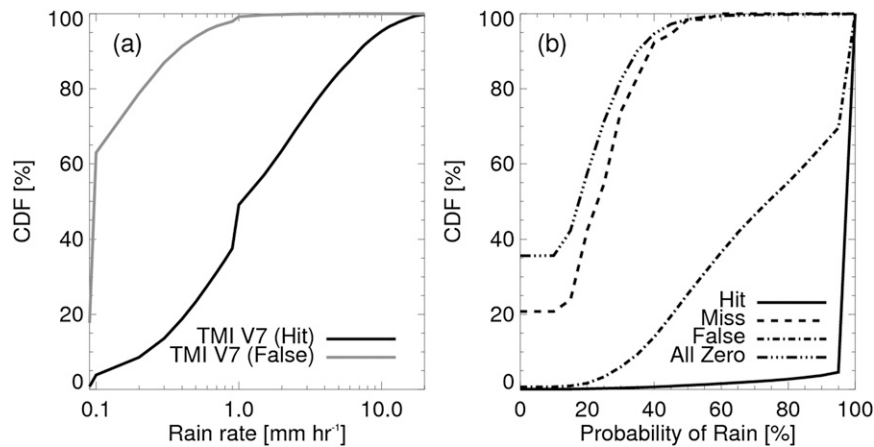
FIG. 10. (a) CDF of pixel-level TMI V7 ocean rain rates from grid boxes defined as hits (black) and false positives (gray). (b) CDF of pixel-level TMI V7 ocean probabilities of rain from grid boxes defined as hits, misses, false rain, and all algorithms equal to zero.

minimum 85-GHz PCT. Overestimation is significant at PCTs of 220 K and below, which confirms the result in Wang et al. (2009), at least for this regime over the southeastern United States. The issue persists in TMI V7, as little to no improvement is observed at low 85-GHz PCTs relative to TMI V6. To improve on the deep convection issue, Gopalan et al. (2010) suggests that additional rain predictors are needed to improve the ice scattering signal and that the TMI–PR collocation method must consider viewing geometries more carefully in convective rainfall.

The relative contribution of this TMI land overestimation to the rain-rate distributions in the rest of the study is addressed in Fig. 13. Grid boxes with an 85-GHz PCT less than 220 K account for only about 4% (5%) of the land (ocean) dataset. As a result, less than 20% of the contribution to the mean rainfall comes from deep convection. The overestimation by the TMI land algorithms adds about a 10% contribution to the mean rain

rate relative to the PR and stage-IV datasets. The greatest contribution to the mean is about linearly distributed between the 220- and 280-K range, which represents average rain rates around 1–10 mm h^{-1} from Fig. 10. The bias distribution in Fig. 12 shows signs of the negative warm bias over land, but this bias does not appear to have a strong influence on the cumulative rainfall contributions.

5. Discussion and conclusions

The two most recent versions of the PR 2A25 and TMI 2A12 rainfall algorithms are compared relative to the reference stage-IV radar–gauge precipitation estimate dataset in landfalling tropical cyclones. The statistical comparison reproduces the most common deficiencies in TRMM version 6 that have been noted by several other studies. Matching the datasets spatially and temporally does add random errors, but the large
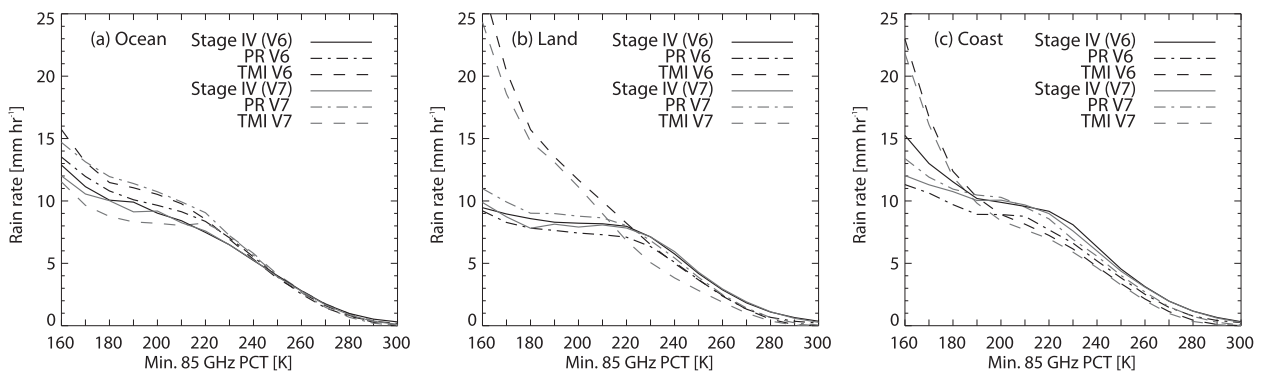

FIG. 11. Distribution of mean rain rates as a function of the minimum 85-GHz PCT (K) in each grid box divided by (a) ocean, (b) land, and (c) coast/mixed surface.
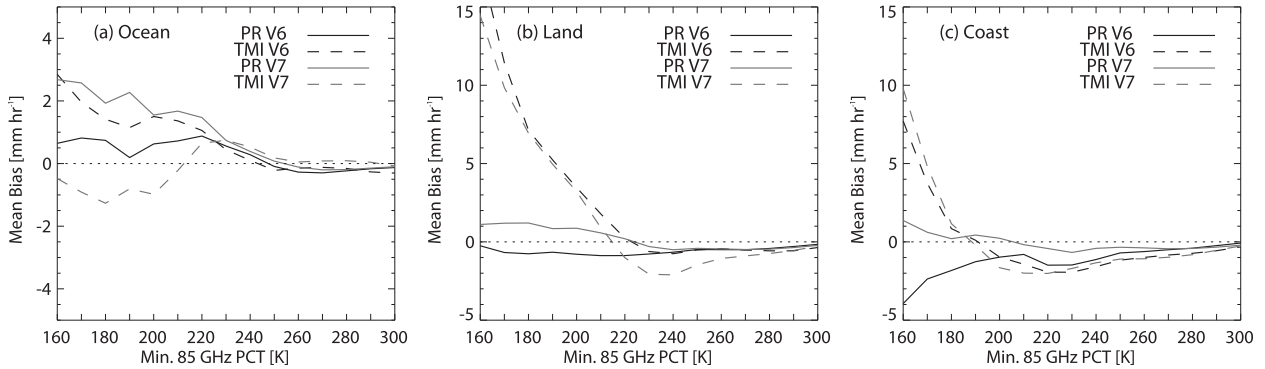
FIG. 12. As in Fig. 11, but for mean bias relative to stage IV.

sample of 252 storms is enough to remove biases related to any individual storm. Even in heavy precipitating systems like TCs, most of the rain rates are light and the heavy rain is concentrated over a relatively small area. Only around 2%–3% of the sample area has a rain rate greater than $10\,\mathrm{mm\,h^{-1}}$, but that small area contributes around 40% of the total rainfall. Identifying the location and intensity of these areas of moderate to heavy rainfall is especially important when forecasting flood threats in landfalling TCs.

The PR V7 algorithm performs the best in all three surface classifications. Over ocean, PR V7 is slightly better than V6, as the hit bias is reduced by two-thirds relative to stage IV. Over land, PR version 7 is again the best-performing algorithm. The remaining PR V7 negative land bias can be mostly explained by underestimation in the 5–$20\,\mathrm{mm\,h^{-1}}$ rain-rate range. It appears that changes to the PR attenuation correction in V7 have removed most of the negative bias at rain rates above $20\,\mathrm{mm\,h^{-1}}$. The PR coastal algorithms both have negative biases of comparable magnitudes to land, with marginal improvement in V7. The PR also underestimates stage IV at light rain rates, an effect of the instrument's inherent minimum reflectivity criteria.

The TMI V7 ocean algorithm is significantly improved relative to V6 in the heavier rain-rate range, $>15\,\mathrm{mm\,h^{-1}}$. The TMI V7 land algorithm is the only instance where V7 has a significantly greater negative bias than V6. Both TMI V6 and V7 land algorithms have much too great of a contribution from light rain rates ($<5\,\mathrm{mm\,h^{-1}}$) and too small of a contribution from moderate rain rates $>5\,\mathrm{mm\,h^{-1}}$. Most of the additional negative bias in V7 comes from the 5–$10\,\mathrm{mm\,h^{-1}}$ rain rates. The main lingering issue with TMI V7 over ocean is the high number of false positives, which must be filtered using the probability of rain parameter. The false positives consist mostly of pixel-level rain rates of 0.1–$0.5\,\mathrm{mm\,h^{-1}}$ and rain probabilities of 50%–100%. Setting a high probability of rain (90%–95%) removes about two-thirds of the false positives while losing less than 5% of the hits.

With respect to ice scattering, the main area where the TMI V7 land algorithm has significant overestimation relative to PR and stage IV is when the minimum 85-GHz PCT is below 220 K. These areas of deep convection are too rare to show up in most of the statistical analysis. One caveat is that the TRMM–stage-IV grid-matching scheme may result in larger errors for these isolated areas of deep convection than for dataset as
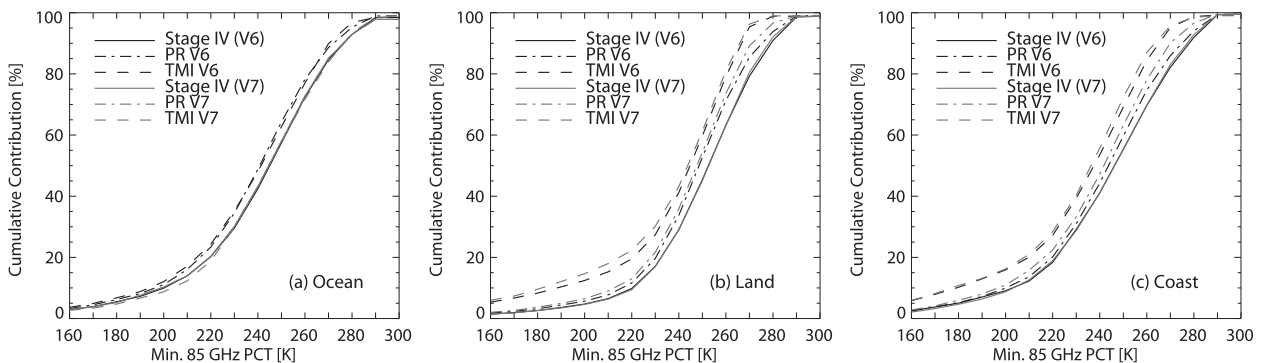

FIG. 13. Cumulative contribution (%) to mean rain rate for TRMM algorithms compared with the minimum 85-GHz PCT divided by (a) ocean, (b) land, and (c) coast/mixed surface.

a whole. The mean PR and stage-IV rain rates of around $10 \, \text{mm h}^{-1}$ (in Fig. 10) for land grid boxes with a minimum 85-GHz PCT $< 200 \, \text{K}$ seem too light. Gopalan et al. (2010) noticed the same issue over several regions including the southern United States. They suggested several possible causes including attenuation and viewing angle discrepancies. Another hypothesis is that upper-level winds may displace the ice scattering downshear of the heaviest rain. Further investigation of the ice scattering–rain rate relationship is required to better understand this discrepancy.

Several lingering questions are raised from this study. First, it is unclear whether the results can be translated to tropical cyclones away from the coastline and in other basins. Island areas may pose different challenges for the coastal algorithm and no high mountainous terrain was within this study's viewing range. The amount of error introduced by comparing instantaneous TRMM overpasses with 1-h stage-IV averages can only be estimated, which makes it hard to make definitive recommendations when the satellite algorithms are close to the reference data. In some instances, the PR appears to be more accurate than stage IV based on visual approximation. Future studies should emphasize detecting raining versus nonraining areas and consider rain gauges as an additional reference dataset.

REFERENCES

Amatai, E., X. Llort, and D. Sempere-Torres, 2009: Comparison of TRMM radar rainfall estimates with NOAA next-generation QPE. *J. Meteor. Soc. Japan,* **87A,** 109–118.

Breidenbach, J. P., and J. S. Bradberry, 2001: Multisensor precipitation estimates produced by National Weather Service River Forecast Centers for hydrologic applications. *Proc. 2001 Georgia Water Resources Conf.,* Athens, GA, University of Georgia, 179–182. [Available online at https://smartech.gatech.edu/xmlui/bitstream/handle/1853/43760/BreidenbachJ-01.pdf?sequence=1.]

Cecil, D. J., and M. Wingo, 2009: Comparison of TRMM rain-rate retrievals in tropical cyclones. *J. Meteor. Soc. Japan,* **87,** 369–380.

——, E. J. Zipser, and S. W. Nesbitt, 2002: Reflectivity, ice scattering, and lightning characteristics of hurricane eyewalls and rainbands. Part I: Quantitative description. *Mon. Wea. Rev.,* **130,** 769–784.

Ebert, E. E., J. E. Janowiak, and C. Kidd, 2007: Comparison of near-real-time precipitation estimates from satellite observations and numerical models. *Bull. Amer. Meteor. Soc.,* **88,** 47–64.

Fulton, R. A., 2002: Activities to improve WSR-88D radar rainfall estimation in the National Weather Service. *Proc. Second Federal Interagency Hydrologic Modeling Conf.,* Las Vegas, NV, Subcommittee on Hydrology of the Advisory Committee on Water Information, 11 pp. [Available online at http://www.nws.noaa.gov/oh/hrl/papers/wsr88d/qpe_hydromodelconf_web.pdf.]

——, J. P. Breidenbach, D.-J. Seo, D. A. Miller, and T. O'Bannon, 1998: The WSR-88D rainfall algorithm. *Wea. Forecasting,* **13,** 377–395.

Gopalan, K., N.-Y. Wang, R. Ferraro, and C. Liu, 2010: Status of the TRMM 2A12 land precipitation algorithm. *J. Atmos. Oceanic Technol.,* **27,** 1343–1354.

Habib, E., A. Henschke, and R. F. Adler, 2009a: Evaluation of TMPA satellite-based research and real-time rainfall estimates during six tropical-related heavy rainfall events over Louisiana, USA. *J. Atmos. Res.,* **94,** 373–388.

——, B. F. Larson, and J. Graschel, 2009b: Validation of NEXRAD multisensor precipitation estimates using an experimental dense rain gauge network in south Louisiana. *J. Hydrol.,* **373,** 463–478.

Huffman, G. J., and Coauthors, 2007: The TRMM Multisatellite Precipitation Analysis (TMPA): Quasi-global, multiyear, combined-sensor precipitation estimates at fine scales. *J. Hydrometeor.,* **8,** 38–55.

Iguchi, T., T. Kozu, R. Meneghini, J. Awaka, and K. Okamoto, 2000: Rain-profiling algorithm for the TRMM precipitation radar. *J. Appl. Meteor.,* **39,** 2038–2052.

Jiang, H., and E. J. Zipser, 2010: Contribution of tropical cyclones to the global precipitation from eight seasons of TRMM data: Regional, seasonal, and interannual variations. *J. Climate,* **23,** 1526–1543.

——, C. Liu, and E. J. Zipser, 2011: A TRMM-based tropical cyclone cloud and precipitation feature database. *J. Appl. Meteor. Climatol.,* **50,** 1255–1274.

Kummerow, C., W. S. Olson, and L. Giglio, 1996: A simplified scheme for obtaining precipitation and vertical hydrometeor profiles from passive microwave sensors. *IEEE Trans. Geosci. Remote Sens.,* **34,** 1213–1232.

——, W. Barnes, T. Kozu, J. Shiue, and J. Simpson, 1998: The Tropical Rainfall Measuring Mission (TRMM) sensor package. *J. Atmos. Oceanic Technol.,* **15,** 809–817.

McCollum, J. R., and R. R. Ferraro, 2005: Microwave rainfall estimation over coasts. *J. Atmos. Oceanic Technol.,* **22,** 497–512.

Mohr, K. I., and E. J. Zipser, 1996: Mesoscale convective systems defined by their 85-GHz ice scattering signature: Size and intensity comparison over tropical oceans and continents. *Mon. Wea. Rev.,* **124,** 2417–2437.

NASA GSFC, 2012: Precipitation processing system—Tropical Rainfall Measuring Mission: File specification for TRMM products, version 7.002, 328 pp. [Available online at http://pps.gsfc.nasa.gov/Documents/filespec.TRMM.V7.pdf.]

Nelson, B. R., D.-J. Seo, and D. Kim, 2010: Multisensor precipitation reanalysis. *J. Hydrometeor.,* **11,** 666–682.

Nesbitt, S. W., E. J. Zipser, and D. J. Cecil, 2000: A census of precipitation features in the tropics using TRMM: Radar, ice scattering, and lightning observations. *J. Climate,* **13,** 4087–4106.

Prat, O. P., and B. R. Nelson, 2013: Precipitation contribution of tropical cyclones in the southeastern United States from 1998 to 2009 using TRMM satellite data. *J. Climate,* **26,** 1047–1062.

Schumacher, C., and R. Houze, 2000: Comparison of radar data from the TRMM satellite and Kwajalein oceanic validation site. *J. Appl. Meteor.,* **39,** 2151–2164.

Seto, S., and T. Iguchi, 2007: Rainfall-induced changes in actual surface backscattering cross sections and effects on rain-rate estimates by spaceborne precipitation radar. *J. Atmos. Oceanic Technol.,* **24,** 1693–1709.

Smith, J. A., D. J. Seo, M. L. Baeck, and M. D. Hudlow, 1996: An intercomparison study of NEXRAD precipitation estimates. *Water Resour. Res.,* **32,** 2035–2045.

Spencer, R. W., H. M. Goodman, and R. E. Hood, 1989: Precipitation retrieval over land and ocean with the SSM/I: Identification and characteristics of the scattering signal. *J. Atmos. Oceanic Technol.,* **6,** 254–273.

Wang, N.-Y., C. Liu, R. Ferraro, D. Wolff, E. Zipser, and C. Kummerow, 2009: TRMM 2A12 land precipitation product—Status and future plans. *J. Meteor. Soc. Japan,* **87A,** 237–253.

Wilheit, T., C. Kummerow, and R. Ferraro, 2003: Rainfall algorithms for the AMSR-E. *IEEE Trans. Geosci. Remote Sens.,* **41,** 204–214.

Willmott, C. J., 1982: Some comments on the evaluation of model performance. *Bull. Amer. Meteor Soc.,* **63,** 1309–1313.

——, S. G. Ackleson, R. E. Davis, J. J. Feddema, K. M. Klink, D. R. Legates, J. O'Donnell, and C. M. Rowe, 1985: Statistics for the evaluation and comparison of models. *J. Geophys. Res.,* **90,** 8995–9005.

Wolff, D. B., and B. L. Fisher, 2008: Comparisons of instantaneous TRMM ground validation and satellite rain-rate estimates at different spatial scales. *J. Appl. Meteor. Climatol.,* **47,** 2215–2237.

——, D. A. Marks, E. Amitai, D. S. Silberstein, B. L. Fisher, A. Tokay, J. Wang, and J. L. Pippitt, 2005: Ground validation for the Tropical Rainfall Measuring Mission (TRMM). *J. Atmos. Oceanic Technol.,* **22,** 365–380.

Zagrodnik, J. P., and H. Jiang, 2013: Properties of TRMM precipitation radar and microwave imager rainfall retrievals in tropical cyclone inner cores and rainbands. *J. Geophys. Res.,* **118,** 29–42, doi:10.1029/2012JD017919.